ATP File Copy

NASA Technical Memorandum 102205

7N-02
175271
p. 27

Low Mach Number Euler Computations

David W. Zingg

(NASA-TM-102205) LOW MACH NUMBER EULER COMPUTATIONS (NASA) 27 p

N93-72473

Unclas

Z9/02 0175271

October 1989

NASA
National Aeronautics and
Space Administration

NASA Technical Memorandum 102205

Low Mach Number Euler Computations

David W. Zingg, University of Toronto, Downsview, Ontario, Canada

October 1989

NASA

National Aeronautics and
Space Administration

Ames Research Center
Moffett Field, California 94035

Summary

Numerical solutions of the Euler equations for two-dimensional airfoil flows at low Mach numbers are compared with analytical solutions for incompressible potential flow. The Euler solutions were obtained using the computer code ARC2D, which employs the Beam and Warming implicit approximate factorization algorithm in generalized coordinates. Analytical solutions for incompressible potential flow were calculated through Joukowsky (cusped trailing edge) and Karman-Trefftz (finite trailing edge angle) transformations. Effects of free-stream Mach number, artificial dissipation, and grid clustering are presented. At a free-stream Mach number of 0.05, the numerical results obtained using a 249 by 49 grid show excellent agreement with the analytical solutions.

1. Introduction

Validation of flow solvers is an important component of the computational fluid dynamics development process. Effects of grid refinement and clustering, numerical dissipation, and turbulence modeling must be understood and quantified. However, when numerical solutions are compared with experimental data, difficulties can arise in distinguishing errors associated with turbulence modeling from those associated with inadequate numerical resolution. Numerical algorithms for the Euler equations are particularly difficult to validate since these equations represent inviscid flow and hence cannot be expected to correspond to experimentally measured flows.

Exact solutions can be obtained for steady, two-dimensional, incompressible potential (i.e., irrotational and inviscid) flow about Joukowsky and Karman-Trefftz airfoils using conformal mappings. The Euler equations reduce to incompressible flow in the limit as the Mach number approaches zero. Therefore, the exact solutions for the incompressible potential flow about Joukowsky and Karman-Trefftz airfoils can be used as test cases to validate computer codes for the Euler equations at low Mach number.

In the present study, numerical solutions of the Euler equations at low Mach numbers for two-dimensional flow about airfoil sections are compared to exact solutions for incompressible potential flow. The purpose of the present study is to assess the accuracy of an Euler code at low Mach number and to investigate the factors affecting the solution. The parameters considered include artificial dissipation, grid clustering, and Mach number. The numerical solutions are obtained for inviscid flow at low Mach number in order to allow comparison with the exact incompressible potential flow cases. The ability of a transonic airfoil code to accurately calculate essentially incompressible flows is a useful feature in itself. Furthermore, it is hoped that some of the

conclusions regarding the effects of grid clustering and artificial dissipation can be extended to higher Mach numbers and to viscous flows.

It is well known that the Euler equations become stiff at very low Mach numbers (ref. 1). The stiffness of the system, which is due to the large ratio between the sound speed and the convective speed, can adversely affect both the accuracy and the efficiency of time-marching methods for the Euler equations. The present study investigates only the accuracy of the low-Mach-number solutions of the Euler equations. No attempt has been made to investigate the effect of the low Mach number on the convergence rate. In order to improve the convergence rate of time-marching methods for the Euler equations at low Mach number, the equations can be preconditioned (refs. 1, 2). However, this approach is only useful for steady-state computations, as the resulting system is no longer time-accurate.

2. Euler Equations

Inviscid compressible flow is governed by the Euler equations. In two dimensions, this system of equations consists of the continuity equation, two momentum equations, and the energy equation. The vector of conservative dependent variables is $[\rho, \rho u, \rho v, e]^T$, where ρ is the local density of the gas, u and v are Cartesian velocity components, and e is the total energy. In strong conservation-law form, the Euler equations are given by

$$\partial_t Q + \partial_x E + \partial_y F = 0 \tag{2.1}$$

where

$$Q = \begin{bmatrix} \rho \\ \rho u \\ \rho v \\ e \end{bmatrix} \qquad E = \begin{bmatrix} \rho u \\ \rho u^2 + p \\ \rho u v \\ u(e+p) \end{bmatrix} \qquad F = \begin{bmatrix} \rho v \\ \rho u v \\ \rho v^2 + p \\ v(e+p) \end{bmatrix} \tag{2.2}$$

For an ideal gas, the pressure is given by the following equation of state:

$$p = (\gamma - 1)[e - \tfrac{1}{2}\rho(u^2 + v^2)] \tag{2.3}$$

where γ, the ratio of specific heats, is generally taken as 1.4.

The dependent variables can be nondimensionalized as follows:

$$\tilde{\rho} = \frac{\rho}{\rho_\infty} \qquad \tilde{u} = \frac{u}{a_\infty} \qquad \tilde{v} = \frac{v}{a_\infty} \qquad \tilde{e} = \frac{e}{\rho_\infty a_\infty^2} \tag{2.4}$$

where a is the sound speed, given by $a^2 = \gamma p / \rho$, and the subscript ∞ denotes free-stream values. With this nondimensionalization, the system of equations is nonsingular in the limit as the Mach number approaches zero.

In Cartesian coordinates, the flux Jacobian matrices $A = \partial E / \partial Q$ and $B = \partial F / \partial Q$ have the following eigenvalues:

$$\Lambda_A = [u,\ u,\ u+a,\ u-a] \qquad \Lambda_B = [v,\ v,\ v+a,\ v-a] \tag{2.5}$$

At very low Mach numbers, the ratio of the eigenvalues involving the sound speed to those involving only the velocity becomes large, and consequently the system becomes stiff.

In irrotational flow, a velocity potential function can be defined by

$$u = \Phi_x \qquad v = \Phi_y \tag{2.6}$$

The continuity equation for incompressible irrotational flow becomes

$$\Phi_{xx} + \Phi_{yy} = 0 \tag{2.7}$$

The pressure is given by the incompressible Bernoulli equation:

$$p + \tfrac{1}{2}\rho_\infty(u^2 + v^2) = p_\infty + \tfrac{1}{2}\rho_\infty(u_\infty^2 + v_\infty^2) \tag{2.8}$$

In a uniform onset flow, solutions to the Euler equations with no shocks or shed vorticity are irrotational and consequently approach the incompressible potential flow solutions as the Mach number approaches zero.

3. Numerical Solution of the Euler Equations

The numerical solutions of the Euler equations presented in this report were obtained using the transonic airfoil code ARC2D. This code employs the Beam and Warming implicit approximate-factorization algorithm in generalized coordinates. A number of options are available in ARC2D with regard to the time-marching method, the artificial dissipation, and reduced forms of the implicit algorithm. Since time-accurate calculations were not required, the present computations were performed using the first-order implicit Euler time-marching method and the diagonal form of the algorithm. Furthermore, since no shocks are present at the low free-stream Mach numbers studied, a nonlinear fourth-order artificial dissipation model was used. The algorithms utilized in ARC2D are described in detail by Pulliam (ref. 3) and are thus only briefly summarized here.

ARC2D solves the Euler equations in generalized curvilinear coordinates. Therefore a procedure is required to produce computational grids about arbitrary two-dimensional airfoils. The grids employed in the present computations were generated using the hyperbolic grid generator described by Barth et al. (ref. 4).

The generalized curvilinear coordinate transformation is given by

$$\tau = t \qquad \xi = \xi(x,y,t) \qquad \eta = \eta(x,y,t) \tag{3.1}$$

The grid spacing is uniform and of unit length in the curvilinear computational space. In generalized curvilinear coordinates, the strong conservation-law form of the Euler equations becomes

$$\partial_\tau \hat{Q} + \partial_\xi \hat{E} + \partial_\eta \hat{F} = 0 \tag{3.2}$$

where

$$\hat{Q} = J^{-1}\begin{bmatrix} \rho \\ \rho u \\ \rho v \\ e \end{bmatrix} \qquad \hat{E} = J^{-1}\begin{bmatrix} \rho U \\ \rho u U + \xi_x p \\ \rho v U + \xi_y p \\ U(e+p) - \xi_t p \end{bmatrix} \qquad \hat{F} = J^{-1}\begin{bmatrix} \rho V \\ \rho u V + \eta_x p \\ \rho v V + \eta_y p \\ V(e+p) - \eta_t p \end{bmatrix} \tag{3.3}$$

U and V are the contravariant velocity components defined as

$$U = \xi_t + \xi_x u + \xi_y v \qquad V = \eta_t + \eta_x u + \eta_y v \tag{3.4}$$

and J is the metric Jacobian, defined as

$$J = (x_\xi y_\eta - x_\eta y_\xi)^{-1} \tag{3.5}$$

Application of the implicit Euler time-marching method to the Euler equations in generalized coordinates gives

$$\Delta\hat{Q}^n + h(\hat{E}_\xi^{n+1} + \hat{F}_\eta^{n+1}) = 0 \tag{3.6}$$

where $\Delta\hat{Q}^n = \hat{Q}^{n+1} - \hat{Q}^n$, $\hat{Q}^n = \hat{Q}(n\Delta t)$, and $h = \Delta t$. Introduction of local time linearizations and approximate factorization leads to the following implicit algorithm:

$$(I + h\partial_\xi \hat{A}^n)(I + h\partial_\eta \hat{B}^n)\Delta\hat{Q}^n = -h(\partial_\xi \hat{E}^n + \partial_\eta \hat{F}^n) = \hat{R}^n \tag{3.7}$$

where $\hat{A} = \partial\hat{E}/\partial\hat{Q}$ and $\hat{B} = \partial\hat{F}/\partial\hat{Q}$ are the flux Jacobians in generalized coordinates.

The partial derivative operators ∂_ξ and ∂_η are approximated using second-order centered differences. Since the mesh spacing in the computational space is uniform and of unit length, the difference operators can be written as

$$\delta_\xi u_{j,k} = \frac{u_{j+1,k} - u_{j-1,k}}{2} \qquad \delta_\eta u_{j,k} = \frac{u_{j,k+1} - u_{j,k-1}}{2} \tag{3.8}$$

where

$$u_{j,k} \equiv u(\xi{=}j, \eta{=}k) \tag{3.9}$$

Linear stability analysis can be used to show that centered differences are nondissipative. The Euler equations also contain no mechanism for dissipation since they represent inviscid flow. However, since the difference operator at a given point involves only the adjacent points, centered differences lead to an odd-even decoupling of grid points. Numerical boundary conditions can excite the odd-even decoupling and the computations can become unstable (ref. 5). The presence of shocks can also lead to instabilities. These instabilities can be controlled using artificial dissipation.

The nonlinear dissipation model developed by Jameson et al. (ref. 6), which combines second- and fourth-difference dissipation, was employed in the present computations. The second-difference dissipation is required only near shocks and consequently was not utilized. The fourth-difference term in the ξ direction is (ref. 3):

$$D_\xi^{(4)} = -\nabla_\xi(\sigma_{j+1,k}\, J_{j+1,k}^{-1} + \sigma_{j,k}\, J_{j,k}^{-1})\, \varepsilon_{j,k}^{(4)}\, \Delta_\xi \nabla_\xi \Delta_\xi Q_{j,k} \tag{3.10}$$

where the one-sided difference operators are defined as

$$\nabla_\xi u_{j,k} = u_{j,k} - u_{j-1,k} \qquad \Delta_\xi u_{j,k} = u_{j+1,k} - u_{j,k} \tag{3.11}$$

The spectral radius of $\hat{A}$, $\sigma_{j,k}$, is given by

$$\sigma_{j,k} = |U| + a\,(\xi_x^2 + \xi_y^2)^{1/2} \tag{3.12}$$

The coefficient $\varepsilon_{j,k}^{(4)}$ is equal to $\kappa_4 \Delta t$ where κ_4 is user-specified. An analogous term is used in the η direction. The dissipation is added to the explicit part of the algorithm as follows:

$$\hat{R}^n = -h\,(\delta_\xi \hat{E}^n + \delta_\eta \hat{F}^n - D_\xi^{(4)} - D_\eta^{(4)}) \tag{3.13}$$

A corresponding implicit operator is obtained by lagging the spectral radius term, thereby linearizing the dissipation. The implicit fourth-difference dissipation operator in the ξ direction is

$$D_i|_\xi = -\nabla_\xi(\sigma_{j+1,k}\, J_{j+1,k}^{-1} + \sigma_{j,k}\, J_{j,k}^{-1})\, \varepsilon_{j,k}^{(4)}\, \Delta_\xi \nabla_\xi \Delta_\xi\, J \tag{3.14}$$

The operator in the η direction has an analogous form. The implicit algorithm can thus be written as

$$(I + h\delta_\xi \hat{A}^n - hD_i|_\xi)(I + h\delta_\eta \hat{B}^n - hD_i|_\eta)\Delta\hat{Q}^n = \hat{R}^n \tag{3.15}$$

Use of the implicit fourth-difference dissipation operator in the implicit algorithm given by equation (3.7) leads to a block pentadiagonal system of equations. The diagonal form of the algorithm described by Pulliam (ref. 3) reduces the system to scalar pentadiagonal form. The steady-state solution is unaffected by the diagonalization.

4. Joukowsky and Karman-Trefftz Transformations

The Joukowsky and Karman-Trefftz transformations are conformal mappings which map a circle in one complex plane to an airfoil in another complex plane. Since the complex potential is known about a circle with arbitrary circulation in a uniform onset flow, the potential flow velocity distributions about Joukowsky and Karman-Trefftz airfoils can be determined analytically. Joukowsky airfoils are characterized by cusped trailing edges while Karman-Trefftz airfoils have finite trailing edge angles. The Joukowsky and Karman-Trefftz transformations are presented in numerous texts (for example, ref. 7) and are thus reviewed only briefly here.

In two-dimensional incompressible potential flow, the velocity components u and v are related to the potential function Φ and the stream function Ψ by the following relations:

$$\Phi_x = u = \Psi_y \qquad \Phi_y = v = -\Psi_x \tag{4.1}$$

The complex potential is defined as

$$F(z) = \Phi(x,y) + i\Psi(x,y) \tag{4.2}$$

where $z = x + iy$. The complex velocity is then given by

$$W(z) \equiv u(x,y) - iv(x,y) = F'(z) \tag{4.3}$$

We now consider a transformation which maps one complex plane, the ζ-plane where $\zeta = \xi + i\eta$, to another complex plane, the z-plane. The flow in the ζ-plane satisfies Laplace's equation (eq. (2.7)) as well as certain prescribed boundary conditions. The flow in the z-plane also satisfies the differential equation and the boundary conditions except at critical points of the transformation. Therefore, simple geometries with known solutions in the ζ-plane can be mapped to complicated geometries in the z-plane. The complex velocity in the z-plane is then given by

$$W[z(\zeta)] = \frac{\tilde{W}(\zeta)}{dz/d\zeta} \tag{4.4}$$

where $\tilde{W}(\zeta)$ is the known complex velocity in the ζ-plane. At critical points of the transformation, i.e., where $dz/d\zeta$ vanishes, the complex velocity in the z-plane becomes infinite unless the complex velocity in the ζ-plane is zero.

The Joukowsky and the Karman-Trefftz transformations both map a circle in the ζ-plane to an airfoil in the z-plane. Figure 1 depicts a circle centered at $\zeta = \mu$ in the ζ-plane. The circle is described by the complex function

$$\zeta = \mu + ae^{i\theta} \tag{4.5}$$

The radius a is chosen such that $\zeta_T = 1$ as shown. The free-stream velocity vector $\mathbf{V}_\infty$ has magnitude V_∞ and is inclined at an angle α to the ξ-axis. The complex velocity for the flow past the circle in the ζ-plane is given by

$$\tilde{W}(\zeta) = V_\infty e^{-i\alpha} + i\frac{\Gamma}{2\pi}\frac{1}{\zeta - \mu} - V_\infty a^2 e^{i\alpha}\frac{1}{(\zeta - \mu)^2} \tag{4.6}$$

where the circulation is defined positive clockwise and has arbitrary magnitude Γ.

In order to map the circle in the ζ-plane to an airfoil with a sharp trailing edge in the z-plane, the transformation $z = z(\zeta)$ must have a critical point at the trailing edge point $\zeta = \zeta_T$. The Kutta condition requires that the complex velocity in the z-plane remain finite at the trailing edge. Therefore, the complex velocity in the ζ-plane must vanish at $\zeta = \zeta_T$, i.e.,

$$\tilde{W}(\zeta = \zeta_T) = 0 \tag{4.7}$$

This condition determines the magnitude of the circulation as

$$\Gamma = 4\pi a V_\infty \sin(\alpha + \beta) \tag{4.8}$$

where β is defined in figure 1. Substituting equations (4.5) and (4.8) into equation (4.6) gives the following expression for the complex velocity distribution on the circle in the ζ-plane:

$$\tilde{W}(\zeta) = i2V_\infty[\sin(\alpha + \beta) - \sin(\alpha - \theta)]e^{-i\theta} \tag{4.9}$$

The Joukowsky transformation is given by

$$z(\zeta) = \zeta + \frac{\zeta_T^2}{\zeta} \tag{4.10}$$

Since we have chosen the radius of the circle a such that $\zeta_T = 1$, the transformation function becomes

$$z(\zeta) = \zeta + \frac{1}{\zeta} \tag{4.11}$$

The derivative of the transformation function is thus

$$\frac{dz}{d\zeta} = 1 - \frac{1}{\zeta^2} \tag{4.12}$$

The camber and thickness of the Joukowsky airfoil are determined by μ, the location of the center of the circle in the ζ-plane. The velocity distribution on the airfoil in the z-plane is given by equation (4.4).

The airfoil sections obtained using the Joukowsky transformation have cusped trailing edges. In order to generate a profile with a finite trailing edge angle, the Karman-Trefftz transformation can be used. With $\zeta_T = 1$, the Karman-Trefftz transformation can be written as

$$\frac{z-n}{z+n} = \frac{(\zeta-1)^n}{(\zeta+1)^n} \tag{4.13}$$

The parameter n determines the trailing edge angle τ as follows:

$$\tau = \pi(2-n) \tag{4.14}$$

Equation (4.13) can be manipulated to give

$$z = n\left[\frac{(\zeta+1)^n + (\zeta-1)^n}{(\zeta+1)^n - (\zeta-1)^n}\right] \tag{4.15}$$

Therefore the derivative of the transformation is

$$\frac{dz}{d\zeta} = \frac{4n^2(\zeta+1)^{n-1}(\zeta-1)^{n-1}}{[(\zeta+1)^n - (\zeta-1)^n]^2} \tag{4.16}$$

The velocity distribution on the airfoil in the z-plane is again given by equation (4.4).

5. Results and Discussion

The present investigations have been carried out using a Joukowsky airfoil and a Karman-Trefftz airfoil. Both airfoils were generated from a circle centered at $\mu = (-0.1, 0.1)$. The parameter n in the Karman-Trefftz transformation was chosen such that the trailing edge angle τ is 10°. The resulting Karman-Trefftz airfoil has a thickness-to-chord ratio of roughly 15%, while the thickness-to-chord ratio of the Joukowsky section is roughly 12%. The airfoils are shown in figure 2. On all figures the coordinates x and y are nondimensional, i.e., they have been scaled by the chord length.

The analytical lift coefficient for the Karman-Trefftz airfoil at zero incidence in incompressible flow is equal to 0.6402. The corresponding value for the Joukowsky airfoil is 0.6231. All of the computational results presented are at zero incidence.

The grids employed are "C" type grids with 249 points in the ξ direction (around the airfoil) and 49 points in the η direction (normal to the airfoil). The distance to the outer boundary is 10 chord lengths. The far-field circulation correction described in reference 3 was used in all of the computations. Grid points are clustered in the ξ direction at the leading and trailing edges. In the η direction, grid points are clustered toward the body. The minimum grid spacing in the ξ direction is equal to the minimum grid spacing in the η direction. Two different grids were generated for each airfoil section. On one grid the minimum point spacing is 0.001 of the airfoil chord while on the second grid it is 0.005 of the chord. These grids will be referred to as the clustered grid and the less clustered grid, respectively. The two grids used for the computations on the Karman-Trefftz airfoil are shown in figures 3a-c and 4a-c. The two grids generated about the Joukowsky airfoil are similar. Unless otherwise specified, the results shown in the figures were computed using the clustered grid.

Lift and quarter-chord pitching moment coefficients computed using the clustered grid on the Karman-Trefftz airfoil are displayed in figures 5 and 6. Also shown are the predictions of linear theory (the Prandtl-Glauert law), which gives

$$C_l = \frac{C_{l_0}}{\beta} \qquad C_m = \frac{C_{m_0}}{\beta} \tag{5.1}$$

where

$$\beta = (1 - M_\infty^2)^{1/2} \tag{5.2}$$

and the subscript 0 refers to incompressible flow. Compared to the linear theory, the lift coefficient and the magnitude of the moment coefficient are slightly overestimated by the computations, even at a free-stream Mach number of 0.05. At such a low free-stream Mach number, the effect of compressibility is virtually negligible, as $\beta = 0.9987$.

Figures 7a-c show the surface pressure distribution on the Karman-Trefftz airfoil at $M_\infty = 0.05$ computed using the clustered grid, in comparison with the analytical result for incompressible flow. The only discrepancy of any significance occurs near the trailing edge, where the loading is slightly overestimated. The computed pressure distribution for the Joukowsky airfoil, shown in figures 8a and 8b, is in slightly better agreement with the theory. Since the Joukowsky airfoil has a cusped trailing edge, the velocity at the trailing edge given by the analytical solution is nonzero. The finite trailing edge angle which characterizes the Karman-Trefftz airfoil produces a stagnation point at the trailing edge. Consequently the pressure gradients near the trailing edge are much higher on the Karman-Trefftz airfoil. The pressure gradients near the trailing edge of the Joukowsky airfoil correspond more closely to those in a viscous flow. The corresponding pressure distributions computed using the less clustered grid are displayed in figures 9a-c and 10a-c. The discrepancies between the theory and the computations are greatly increased.

In subcritical inviscid flow, the drag on an airfoil section is zero. For inviscid flow, the drag is calculated in ARC2D by numerically integrating the appropriate component of the pressure force

about the airfoil. This procedure is very sensitive to errors in the computed pressure distribution since relatively large pressure forces must cancel to produce zero drag. Therefore, in subcritical inviscid flow, the drag coefficient is a useful measure of the accuracy of a computed flow field.

The pressure distributions computed using the less clustered grid displayed in figures 9 and 10 produce drag coefficients greater than 0.001. The drag coefficients computed using the clustered grid are generally below 0.0003, depending on the amount of artificial dissipation used. The dependence of the drag coefficients computed at $M_\infty = 0.05$ on the artificial dissipation is displayed in figure 11. The dissipation parameter shown in the figures is equal to 64 times the artificial dissipation coefficient κ_4, which is defined following equation (3.12). Therefore a value of the dissipation parameter shown on the figures equal to 0.64 corresponds to $\kappa_4 = 0.01$, which is the typical value given by Pulliam (ref. 3). Figure 11 shows that the computed drag coefficient at $M_\infty = 0.05$ is very sensitive to the artificial dissipation coefficient. The value of κ_4 which produces the minimum drag coefficient is 0.00125, far less than the typical value. At $M_\infty = 0.4$, the computed drag coefficient is much less sensitive to the value of the dissipation coefficient, as shown in figure 12. Although a value of κ_4 equal to 0.0025 minimizes the drag at this Mach number, the drag coefficient computed using the typical value of 0.01 is not significantly higher.

The variation of the computed drag coefficient with free-stream Mach number is shown in figure 13. In each case the value of the artificial dissipation coefficient which minimizes the drag was used. The computed drag coefficient increases with decreasing Mach number. This suggests that the solution accuracy is somewhat degraded at very low Mach numbers.

The odd-even decoupling of grid points characteristic of centered-difference schemes is displayed in figure 14, which shows the coefficient of pressure contours on the Karman-Trefftz airfoil at $M_\infty = 0.05$ computed using a value of the dissipation coefficient κ_4 equal to 0.00125. Increasing κ_4 to 0.01 eliminates the odd-even decoupling entirely, as shown in figure 15, but produces a higher drag coefficient. Figures 16a and 16b show that the surface pressure distribution is computed more accurately using $\kappa_4 = 0.00125$. Increasing the value of κ_4 leads to oscillations in the surface pressure distribution near the trailing edge.

The entropy field is another useful measure of the accuracy of a numerical solution. In subcritical inviscid flow, no entropy should be generated. Figures 17 and 18 show the entropy, s, generated on the surface of the Karman-Trefftz airfoil at $M_\infty = 0.05$ with κ_4 equal to 0.00125 and 0.01, respectively. The higher value of the dissipation coefficient leads to an increase in entropy generation. This is consistent with the increased drag computed using $\kappa_4 = 0.01$. Figure 19 shows that the less clustered grid leads to considerably increased entropy levels, again consistent with the high value of drag computed for this case. Hence, the entropy field is a useful error measure for grid assessment.

Finally, a 497 by 97 grid was generated about the Karman-Trefftz airfoil. The minimum grid spacing in both the ξ and η directions was reduced to one half of the minimum grid spacing on the clustered 249 by 49 grid, i.e., a minimum grid spacing of 0.0005 of the chord was used. Note that this grid is not formally a factor-of-two refinement of the clustered 249 by 49 grid, as the same relative point distribution has not been maintained. Using this refined grid, the drag coefficient on

the Karman-Trefftz airfoil at $M_\infty = 0.05$ computed with $\kappa_4 = 0.00125$ is reduced to a value below 0.0001, i.e, the computed drag is reduced by a factor of 3.2 compared to the drag computed using the clustered 249 by 49 grid. The error obtained by comparing the computed lift coefficient with the value given by linear theory at $M_\infty = 0.05$ is reduced from 0.5% to 0.4% using the refined grid. The error reduction in the computed pitching moment coefficient is similar.

6. Conclusions

Numerical solutions of the Euler equations for two-dimensional airfoil flows at low Mach numbers have been compared to analytical solutions for incompressible potential flow obtained using conformal mapping theory. The Euler solutions were obtained using the computer code ARC2D, which employs the Beam and Warming approximate factorization algorithm in generalized coordinates. Based on the comparisons, the following conclusions can be drawn:

1. The Beam and Warming algorithm can be used to compute accurate solutions to the Euler equations at free-stream Mach numbers down to 0.05. At such a low Mach number, the flow is virtually incompressible.
2. Solution accuracy can be greatly degraded if the numerical grid is insufficiently clustered in appropriate regions.
3. Solution accuracy is somewhat degraded at Mach numbers below 0.2 and the solutions are sensitive to the amount of artificial dissipation used. As the Mach number is increased, the influence of the artificial dissipation level is reduced.
4. Both the drag coefficient and the entropy field are useful measures of the accuracy of a computed solution in subcritical inviscid flow. The entropy field is particularly useful for grid assessment.

7. References

1. Turkel, E.: Preconditioned Methods for Solving the Incompressible and Low Speed Compressible Equations. NASA CR-178086, ICASE Rep. 86-14, Mar. 1986.
2. Briley, W.R.; McDonald, H.; and Shamroth, S.J.: A Low Mach Number Euler Formulation and Application to Time-Iterative LBI Schemes. AIAA J., vol. 21, no. 10, Oct. 1983.
3. Pulliam, T.H.: Efficient Solution Methods for the Navier-Stokes Equations. Lecture Notes for the Von Karman Institute for Fluid Dynamics Lecture Series: Numerical Techniques for Viscous Flow Computation in Turbomachinery Bladings. Jan. 20-24, 1986, Von Karman Institute for Fluid Dynamics, Brussels, Belgium.
4. Barth, T.J.; Pulliam, T.H.; and Buning, P.G.: Navier-Stokes Computations for Exotic Airfoils. AIAA Paper 85-0109, Jan. 1985.
5. Pulliam, T.H.: Artificial Dissipation Models for the Euler Equations. AIAA J., vol. 24, no. 12, Dec. 1986.
6. Jameson, A.; Schmidt, W.; and Turkel, E.: Numerical Solutions of the Euler Equations by Finite Volume Methods Using Runge-Kutta Time-Stepping Schemes. AIAA Paper 81-1259, June 1981.
7. Karamcheti, K.: Principles of Ideal-Fluid Aerodynamics. John Wiley & Sons, New York, 1966.

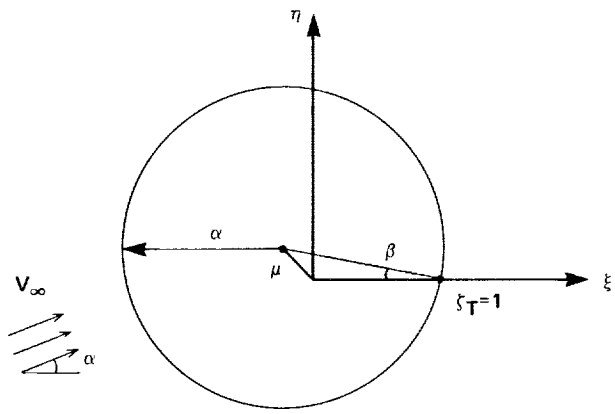

Figure 1.– Circle in the ζ-plane.

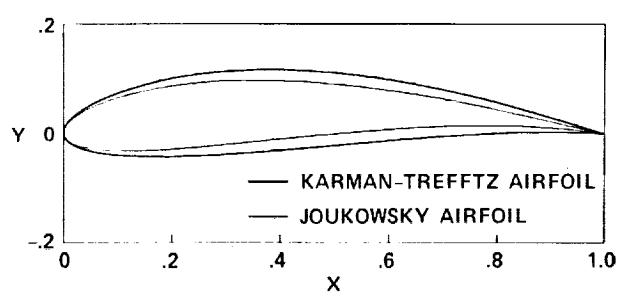

Figure 2.– Airfoil sections.

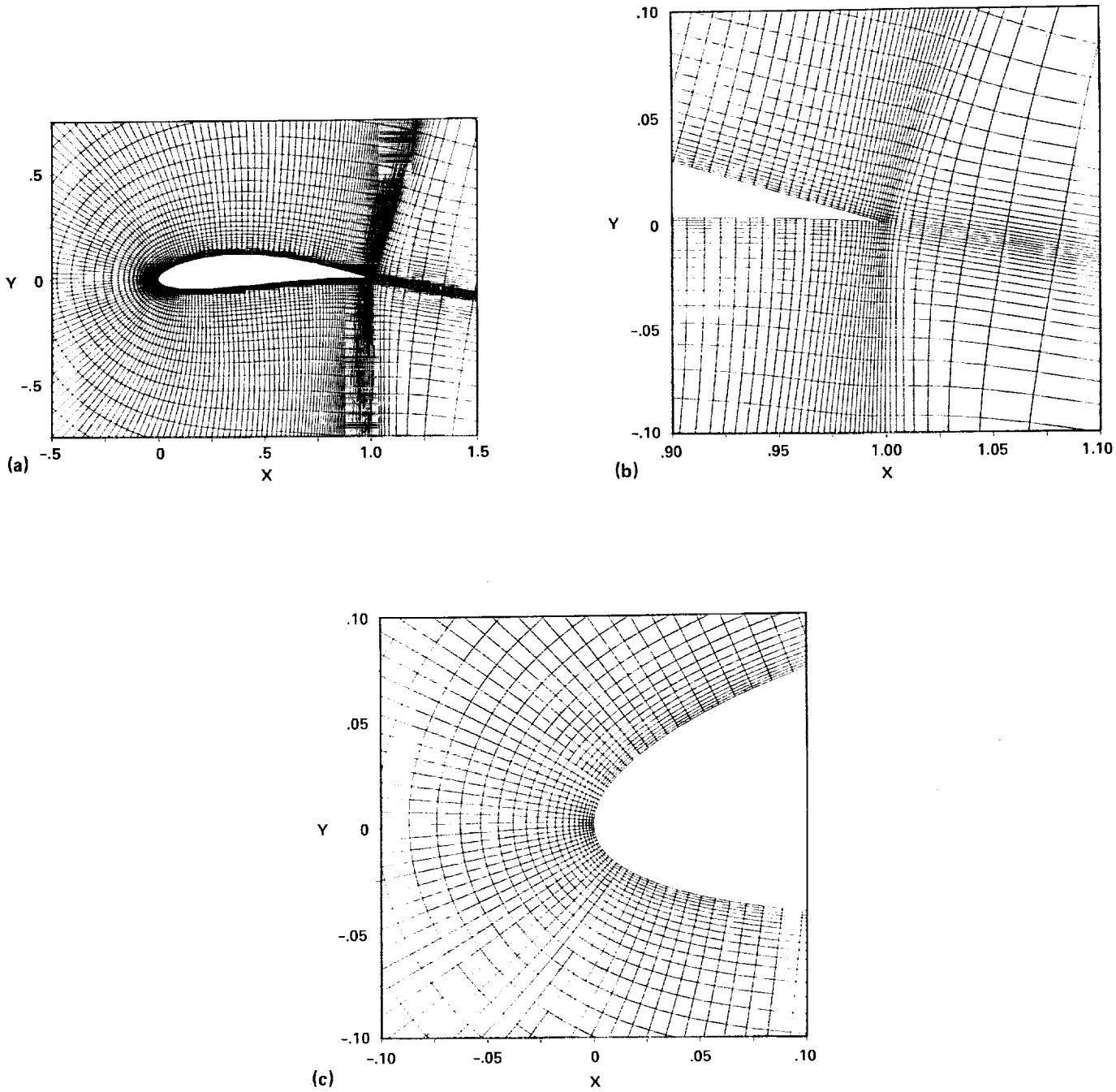

Figure 3.– Clustered grid generated about Karman-Trefftz airfoil, near (a) Entire airfoil, (b) Trailing edge, (c) Leading edge.

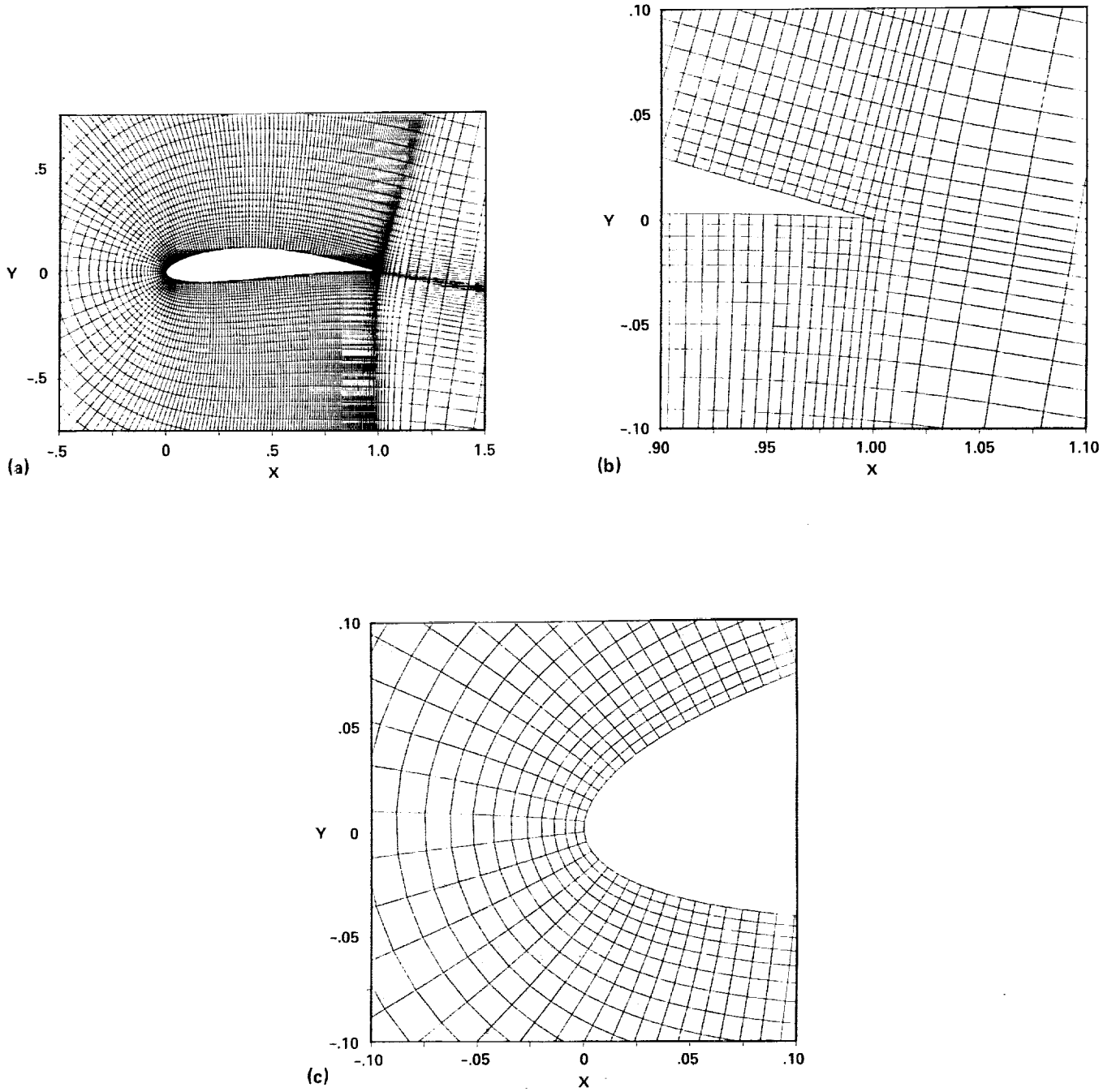

Figure 4.– Less clustered grid generated about Karman-Trefftz airfoil, near (a) Entire airfoil, (b) Trailing edge, (c) Leading edge.

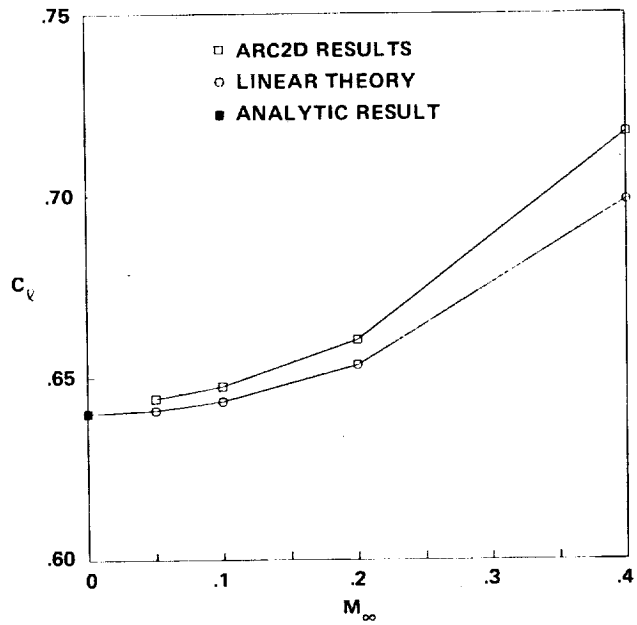

Figure 5.– Variation of lift coefficient with free-stream Mach number, Karman-Trefftz airfoil.

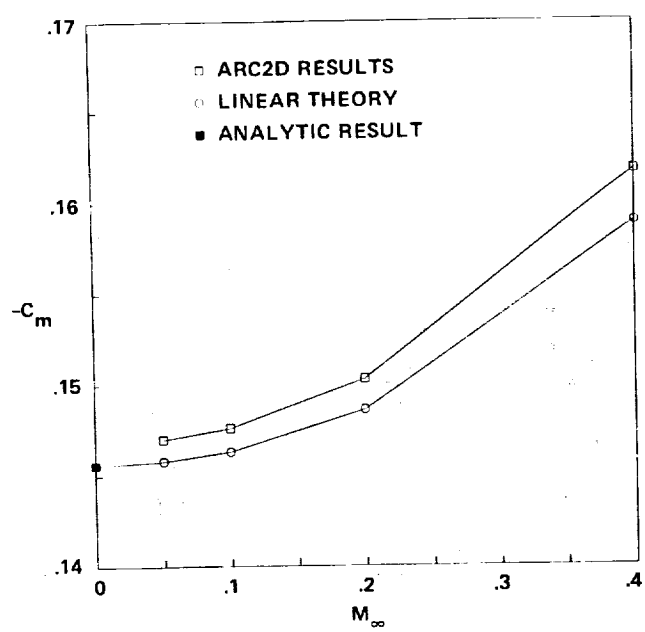

Figure 6.– Variation of pitching moment coefficient with free-stream Mach number, Karman-Trefftz airfoil.

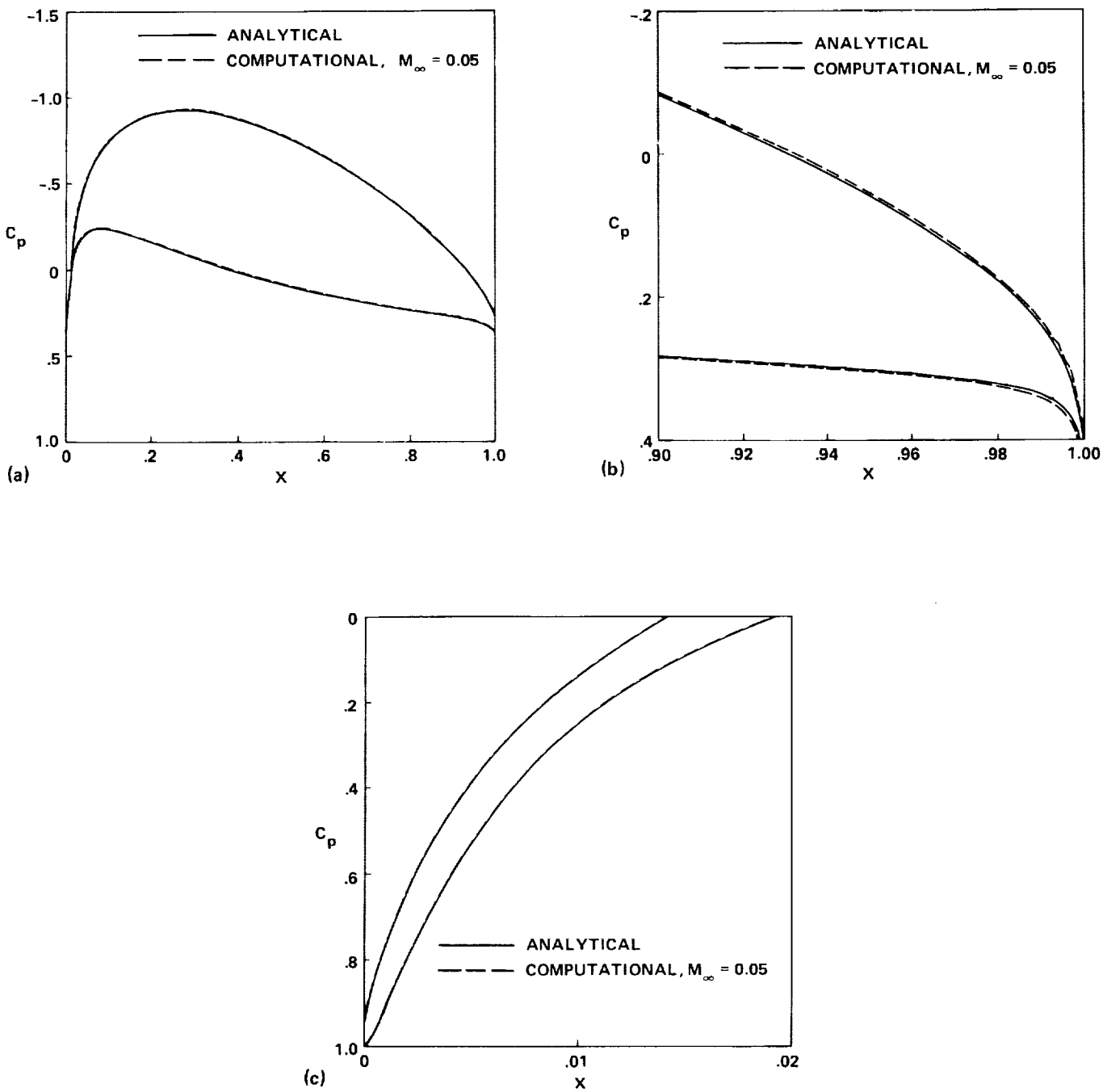

Figure 7.– Computational and analytical surface pressure distributions, Karman-Trefftz airfoil, clustered grid (a) On entire airfoil, (b) Near trailing edge, (c) Near leading edge.

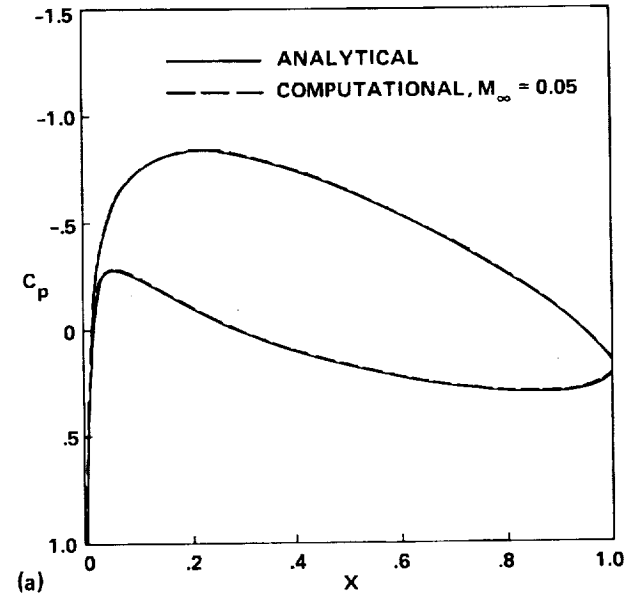

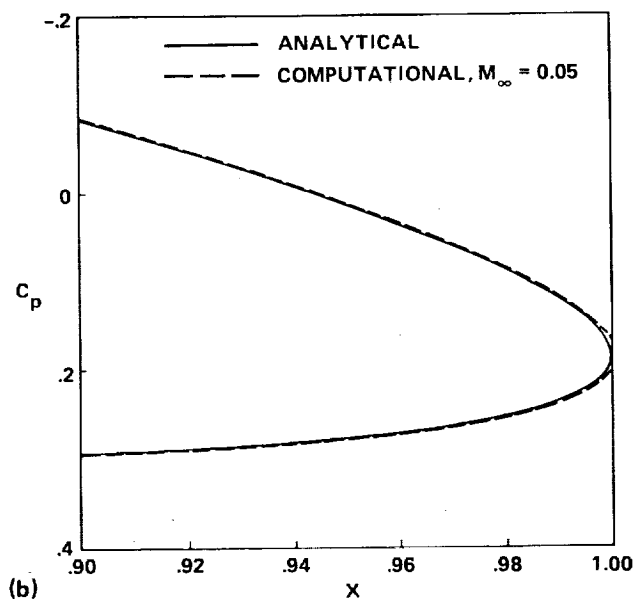

Figure 8.– Computational and analytical surface pressure distributions, Joukowsky airfoil, clustered grid (a) On entire airfoil, (b) Near trailing edge.

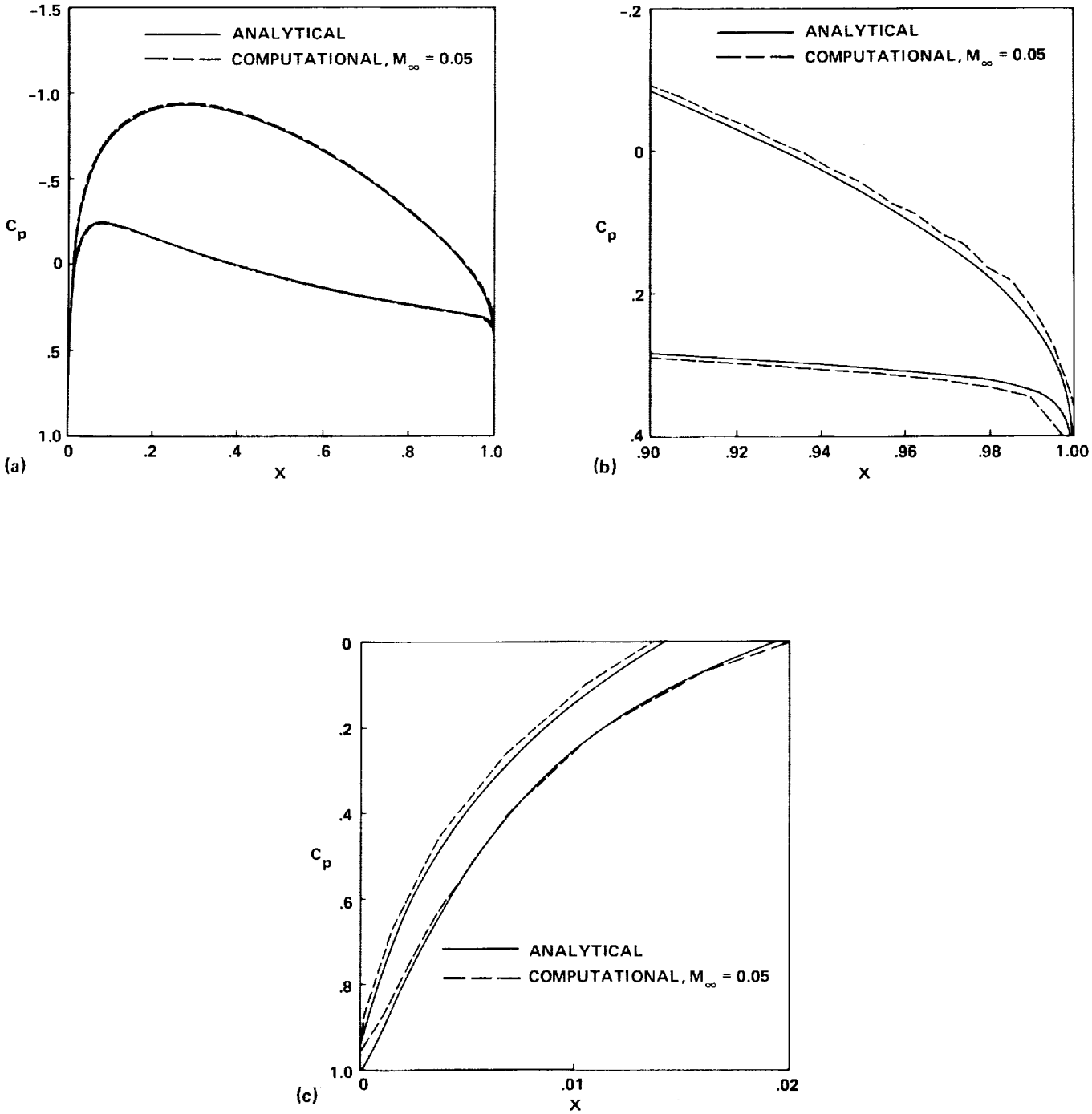

Figure 9.– Computational and analytical surface pressure distributions, Karman-Trefftz airfoil, less clustered grid (a) On entire airfoil, (b) Near trailing edge, (c) Near leading edge.

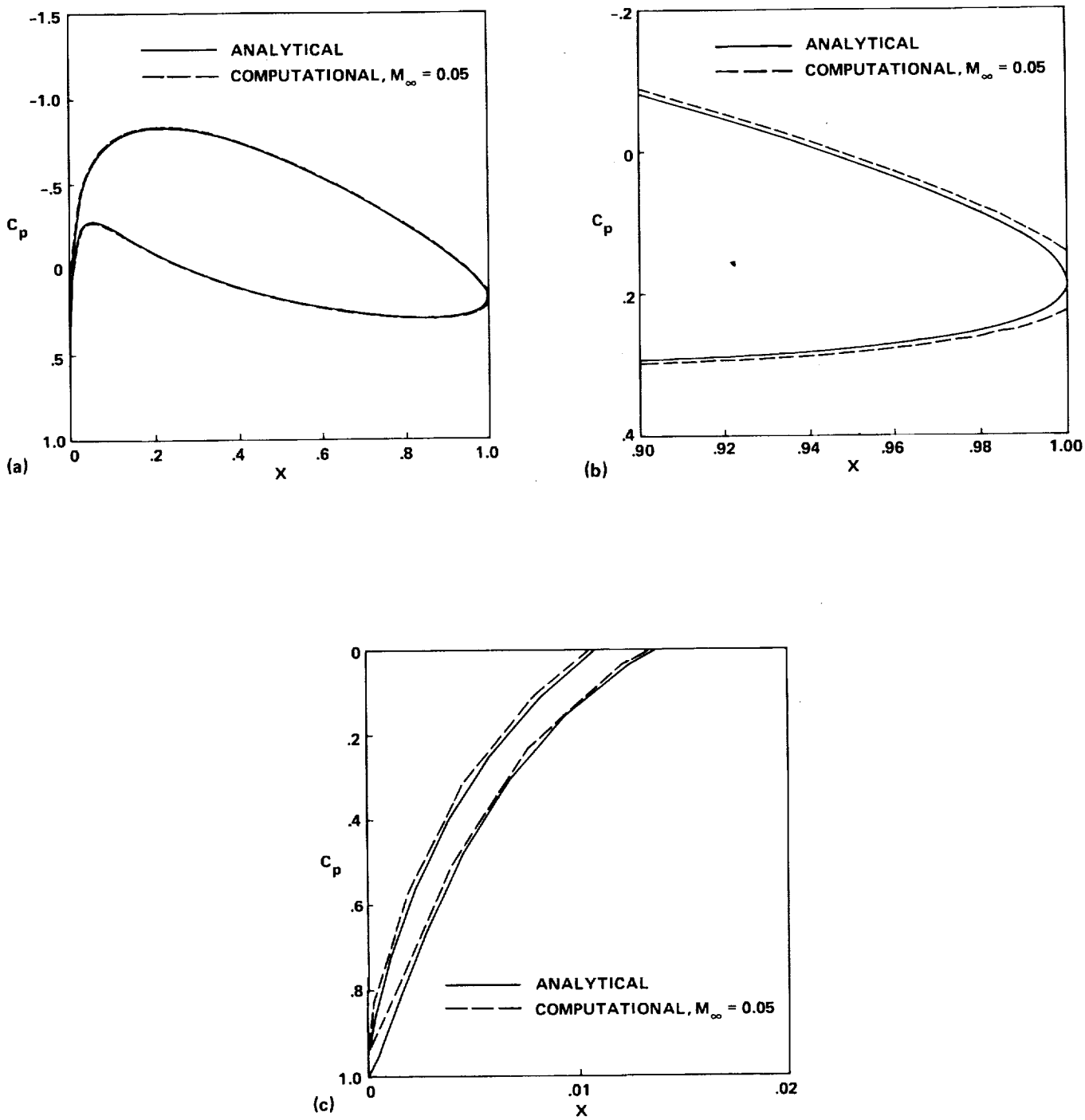

Figure 10.– Computational and analytical surface pressure distributions, Joukowsky airfoil, less clustered grid (a) On entire airfoil, (b) Near trailing edge, (c) Near leading edge.

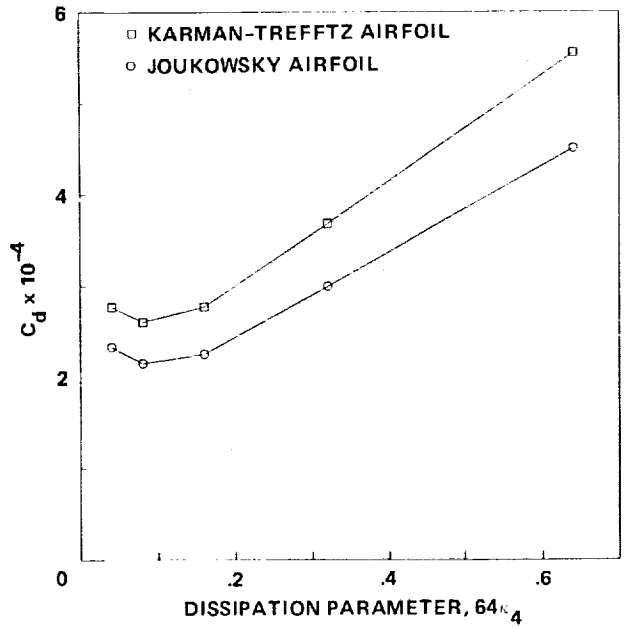

Figure 11.– Variation of computed drag coefficient with artificial dissipation coefficient, $M_\infty = 0.05$.

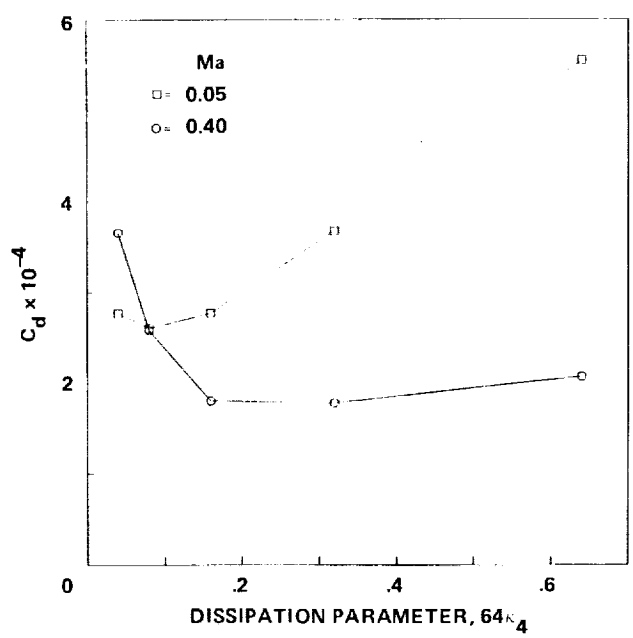

Figure 12.– Variation of computed drag coefficient with artificial dissipation coefficient, Karman-Trefftz airfoil.

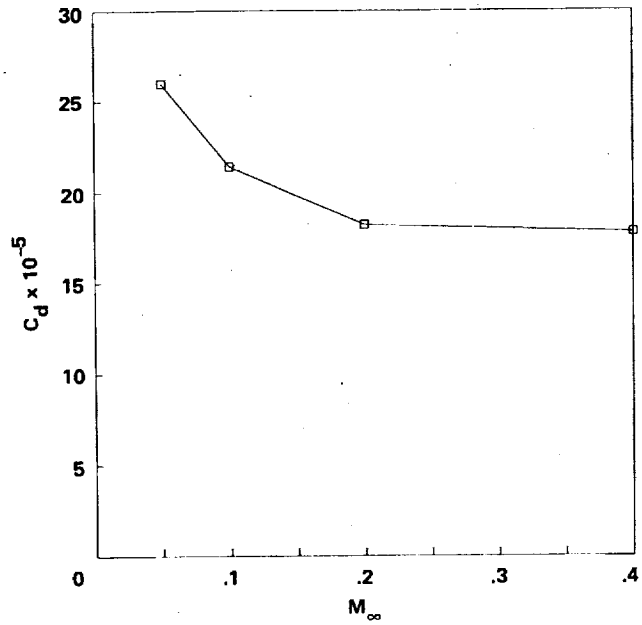

Figure 13.– Variation of computed drag coefficient with free-stream Mach number, Karman-Trefftz airfoil.

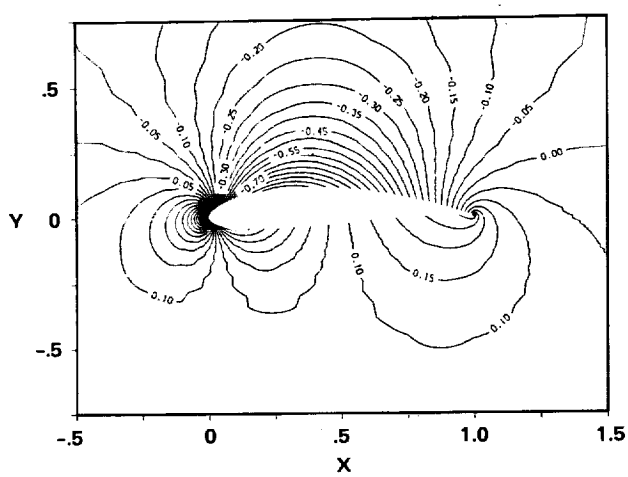

Figure 14.– Coefficient of pressure contours, Karman-Trefftz airfoil, $M_\infty = 0.05$, $\kappa_4 = 0.00125$.

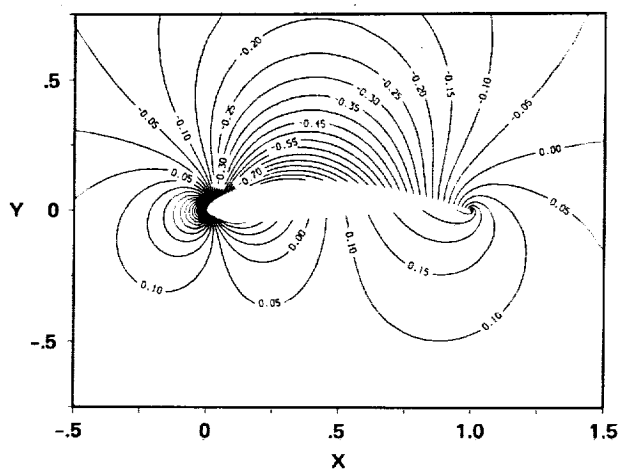

Figure 15.– Coefficient of pressure contours, Karman-Trefftz airfoil, $M_\infty = 0.05$, $\kappa_4 = 0.01$.

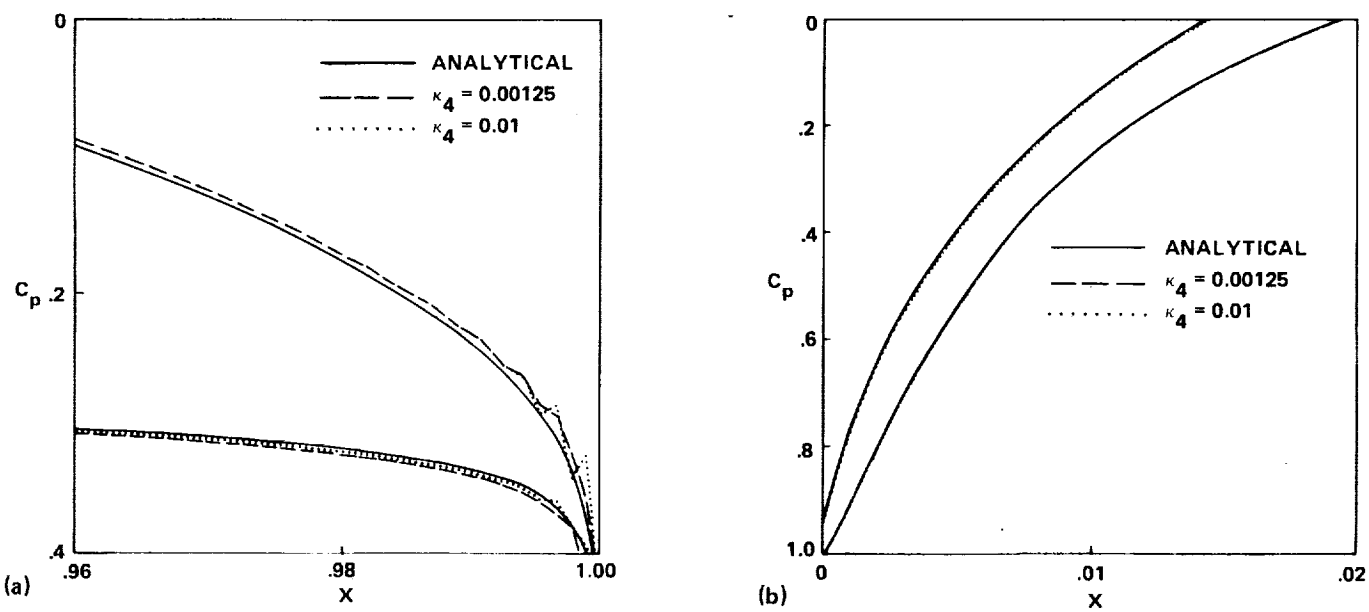

Figure 16.– Computational and analytical surface pressure distributions, Karman-Trefftz airfoil, $M_\infty = 0.05$, near (a) Trailing edge, (b) Leading edge.

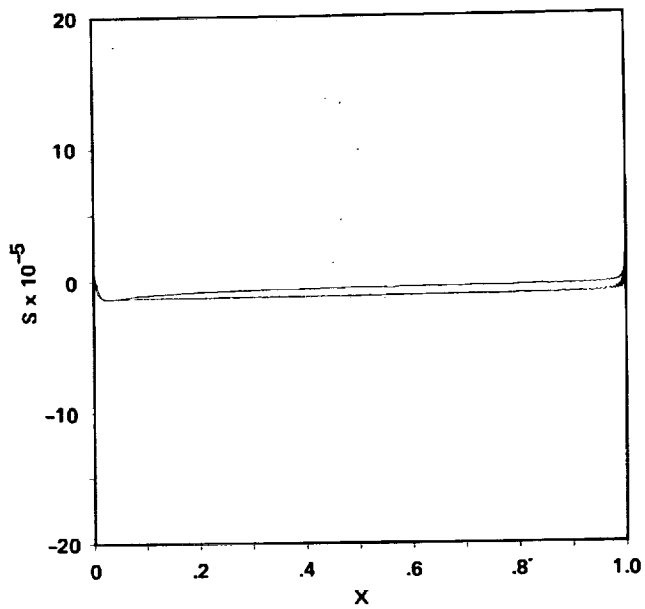

Figure 17.– Computed surface entropy distribution, Karman-Trefftz airfoil, $M_\infty = 0.05$, $\kappa_4 = 0.00125$.

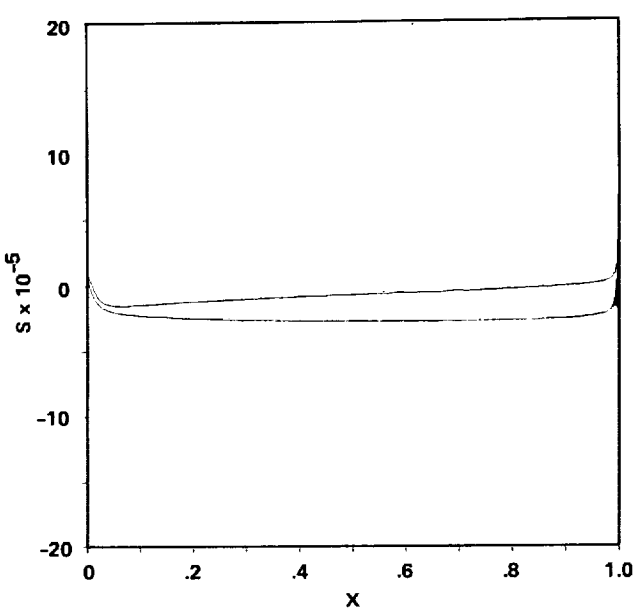

Figure 18.– Computed surface entropy distribution, Karman-Trefftz airfoil, $M_\infty = 0.05$, $\kappa_4 = 0.01$.

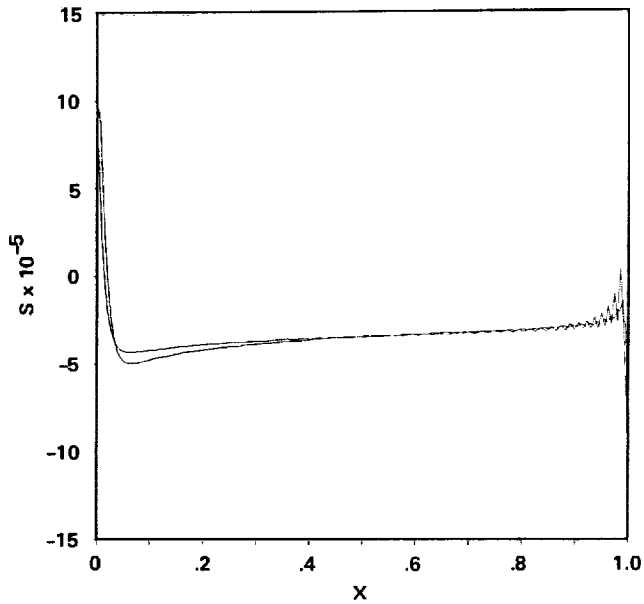

Figure 19.– Computed surface entropy distribution, Karman-Trefftz airfoil, $M_\infty = 0.05$, $\kappa_4 = 0.00125$, less clustered grid.

NASA
National Aeronautics and Space Administration

Report Documentation Page

1. Report No. NASA TM-102205	2. Government Accession No.	3. Recipient's Catalog No.
4. Title and Subtitle Low Mach Number Euler Computations		5. Report Date October 1989
		6. Performing Organization Code
7. Author(s) David W. Zingg (University of Toronto, Downsview, Ontario, Canada)		8. Performing Organization Report No. A-89192
		10. Work Unit No. 505-60
9. Performing Organization Name and Address Ames Research Center Moffett Field, CA 94035		11. Contract or Grant No.
		13. Type of Report and Period Covered Technical Memorandum
12. Sponsoring Agency Name and Address National Aeronautics and Space Administration Washington, DC 20546-0001		14. Sponsoring Agency Code

15. Supplementary Notes

Point of Contact: Thomas Pulliam, Ames Research Center, MS 202A-1, Moffett Field, CA 94035 (415) 694-6417 or FTS 464-6417

16. Abstract

Numerical solutions of the Euler equations for two-dimensional airfoil flows at low Mach numbers are compared with analytical solutions for incompressible potential flow. The Euler solutions were obtained using the computer code ARC2D, which employs the Beam and Warming implicit approximate factorization algorithm in generalized coordinates. Analytical solutions for incompressible potential flow were calculated through Joukowsky (cusped trailing edge) and Karman-Trefftz (finite trailing edge angle) transformations. Effects of free-stream Mach number, artificial dissipation, and grid clustering are presented. At a free-stream Mach number of 0.05, the numerical results obtained using a 249 by 49 grid show excellent agreement with the analytical solutions.

17. Key Words (Suggested by Author(s)) Euler computations Airfoil computations Incompressible flow	18. Distribution Statement Unclassified-Unlimited Subject Category - 02

19. Security Classif. (of this report) Unclassified	20. Security Classif. (of this page) Unclassified	21. No. of Pages 25	22. Price A02

NASA FORM 1626 OCT 86

For sale by the National Technical Information Service, Springfield, Virginia 22161